

# Microwave generation from rotating electron beams in magnetron-type waveguides

W. W. Destler, R. Kulkarni, C. D. Striffler, and R. L. Weiler  
University of Maryland, College Park, Maryland 20742

(Received 27 January 1983; accepted for publication 1 April 1983)

The production of high power microwave radiation at high harmonics of the electron cyclotron frequency by the interaction of a rotating electron beam with a magnetron-type conducting boundary has been studied theoretically and experimentally using a 2-MeV, 1–2-kA, 10-ns electron beam pulse. Approximately 10% of the electron beam power has been converted to microwave radiation at the 12th harmonic, and about 2% at the 20th harmonic. Radiation characteristics are in good agreement with a theoretical analysis of the resonant interaction of a beam mode with the modes of the conducting boundary system. Radiation from rotating beams in “glide-symmetric” boundary systems is also reported.

PACS numbers: 85.10.Ka

## I. INTRODUCTION

The renewed interest in novel high power microwave/millimeter wave sources in the past few years has resulted from possible applications of such sources in such diverse areas as heating of fusion plasmas, particle accelerators, and communications. Among these new sources are gyrotrons,<sup>1–3</sup> free electron lasers,<sup>4,5</sup> and relativistic magnetrons.<sup>6,7</sup> In this paper, we report experimental and theoretical studies of a new type of microwave device in which high power microwaves are generated at high harmonics of the electron cyclotron frequency ( $\omega_c$ ) by the injection of a rotating, axis encircling, electron layer (*E*-layer) into a magnetron-type conducting boundary configuration. This concept, first reported by our group in 1981,<sup>8</sup> was derived from previous experimental and theoretical work on the microwave production from rotating *E*-layers in simple cylindrical or coaxial boundary systems.<sup>9,10</sup>

The potential of such devices to produce radiation at or near high harmonics of the electron cyclotron frequency makes them especially attractive, since they require substantially less applied magnetic field strength than gyrotrons or magnetrons operating at the same frequency. Recent theoretical studies,<sup>11–13</sup> moreover, indicate that they may be expected to operate over a wide range of electron energies and currents and at frequencies into the millimeter regime. In this paper, we present theoretical and experimental studies of the production of radiation in such systems at or near  $12\omega_c$  and  $20\omega_c$ . In addition, we discuss the results of an experiment in which an *E*-layer is injected into a “glide symmetric” boundary system designed to produce radiation near the 40th harmonic. A theoretical discussion in which the radiation is modeled as a resonant interaction of a beam mode with the modes of the conducting boundary system is presented in Sec. II. The experimental results are summarized in Sec. III, and conclusions are drawn in Sec. IV.

## II. ANALYSIS OF THE INTERACTION OF AN ELECTRON BEAM WITH A SLOTTED WAVEGUIDE: CARTESIAN LIMIT ( $k_z = 0$ )

In our experiment, a thin annular electron beam rotates about the axis of a magnetic field ( $B_0$ ) slotted waveguide cy-

lindrical system as shown in Fig. 1(a). The beam's azimuthal velocity is

$$V_\phi = R_B \omega_c = \frac{R_B e B_0}{m \gamma_0}$$

and also has a velocity component along the field  $V_z$ , where

$$\beta_\phi^2 + \beta_z^2 = (V_\phi/c)^2 + (V_z/c)^2 = 1 - (1/\gamma_0^2).$$

The slotted structure is placed on either the outer wall, the inner wall, or both. In order to investigate theoretically the interaction of the beam with the modes of the guide, we have considered a cartesian model of the cylindrical system. This

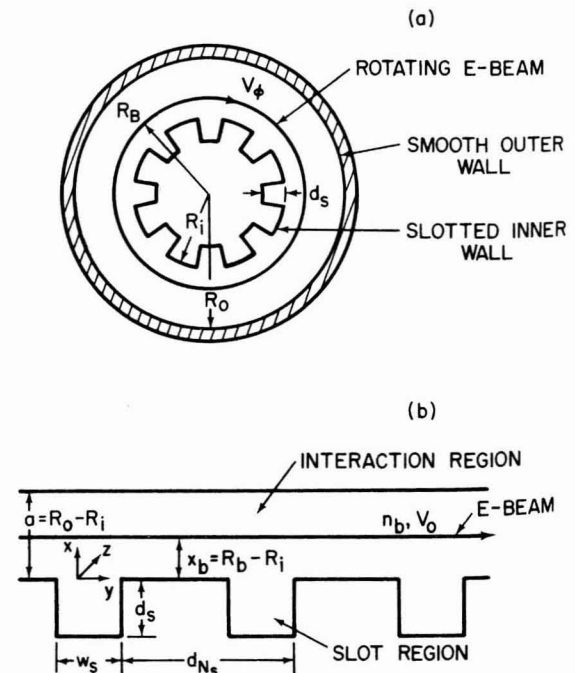


FIG. 1. (a) Experimental schematic of inner slotted coaxial waveguide with  $N_s$  slots. (b) Cartesian model of the cylindrical waveguide as a periodic planar system of  $N_s$  slots.

model is shown in Fig. 1(b). The model and dimensions are so drawn and labeled as if the slotted wall is interior to the beam and the exterior wall is smooth. The space where the beam travels, the "interaction region," has a width "a" ( $= R_0 - R_i$ ) and the slots have a depth  $d_s$ , width  $w_s$ , and a periodicity given by the length  $d_{N_s}$ . The symbol  $N_s$  represents the number of the slots in the cylindrical system, that is, we require  $N_s d_{N_s} = 2\pi R_B$ . Thus, in the cartesian analysis, the system periodicity occurs in a distance  $N_s d_{N_s}$ . The beam is located a distance  $x_b (= R_b - R_i)$  from the slots and is travelling across the slots at a velocity  $V_0 (= V_\phi)$ . The coordinate system for analysis is also shown in Fig. 1(b).

A brief comment on the cartesian model is in order because of the large amount of literature, including our own,<sup>10</sup> that analyzed the smooth wall tube in cylindrical coordinates. In the smooth wall case, the analysis of mode structure and linear stability of the interaction of the rotating electron beam with the waveguide modes was relatively straightforward. For smooth walls, cylindrical waveguides are required in order to have any mode-beam resonance. In that case, the linearized quantities were Fourier decomposed as  $\exp(i\phi + k_z z - \omega t)$ . The dominant perturbation in that case was along the beam, and we obtained<sup>10</sup>

$$R_B \tilde{\phi}_1 \simeq \frac{e}{m\gamma_0} \frac{(\psi_i^2/\gamma_{\phi 0}^2 + \omega_c^2 \beta_{\phi 0}^2)}{\psi_i^2 - \omega_c^2} \frac{\delta \tilde{E}_\phi}{\psi_i^2}, \quad (1)$$

where  $\psi_i = \omega - l\omega_c - k_z V_{z0}$ ,  $\omega_c = eB_0/m\gamma_0$ ,  $\beta_{\phi 0} = R_B \omega_c/c$ ,  $\gamma_0 = (1 - \beta_{\phi 0}^2 - \beta_{z0}^2)^{-1/2}$ . When analyzing resonant interaction  $\psi_i \simeq 0$ , the above expression can be approximated by

$$r_0 \tilde{\phi}_1 \simeq - \frac{e}{m\gamma_0} \beta_{\phi 0}^2 \frac{\delta \tilde{E}_\phi}{\psi_i^2}, \quad (2)$$

which represents a "negative mass" effect. However, if the above analysis is taken to the cartesian limit,  $V_{\phi 0} = R_B \omega_c = \text{constant}$ ,  $R_b \rightarrow \infty$ ,  $B_0 \rightarrow 0$ , Eq. (1) becomes

$$R_B \tilde{\phi}_1 \simeq \frac{e}{m\gamma_0} \frac{1}{\gamma_{\phi 0}^2} \frac{\delta \tilde{E}_\phi}{\psi_i^2}, \quad (3)$$

now representing a "positive mass." Below, we will derive an expression identical to Eq. (3). With respect to the analysis at hand where we are looking for resonant interaction of a

beam wave with a waveguide mode, the sign of the mass term is not important, since the equation is cubic versus quadratic in form. Likewise, the dominance of the negative mass term or the cartesian term for a given system is not clear. The magnitude of  $\gamma_0$ , location of the beam relative to the conducting wall, frequency shift, and beam density ( $v/\gamma_0$ ), all appear to be determining factors as to which is most important. However, the relative simplicity of the modes for a cartesian slotted waveguide versus the actual cylindrical slotted waveguide has led us to pursue the former model.

### A. Empty waveguide analysis: Dispersion relation

In this initial investigation, we simplify the analysis by considering the mode structure for the case of  $k_z = 0$  (cut-off). When there is no beam present, the empty waveguide, the modes decompose into TE and TM waves. Only the TE mode ( $E_z = 0$ ,  $H_z \neq 0$ ) has a nonzero value of  $E_y$ , the electric field that couples the wave to the beam. Assuming the fields vary as  $\exp(j\omega t - j\beta_n y)$ , the  $H_z$  field in the interaction region,  $0 < x < a$ , is given by

$$H_z^I(x, y) = \sum_{n=-\infty}^{\infty} A_n \cos[K_n(a-x)] e^{-j\beta_n y}, \quad (4)$$

where  $K_n^2 = \omega^2/c^2 - \beta_n^2$ ,  $\beta_n = \beta_0 + 2\pi n/d_{N_s}$ , and the other nonzero fields are given by  $E_x^I = -(\beta_n/\omega\epsilon_0)H_z^I$  and  $E_y^I = (j/\omega\epsilon_0)\partial H_z^I/\partial x$ . The quantity  $\beta_0 d_{N_s}$  represents the phase shift from one slot region to the next. Likewise, in the first slot region,  $-d_s < x < 0$ ,  $-w_s/2 < y < w_s/2$ , the  $H_z$  field is given by

$$H_z^s(x, y) = \sum_{n'=0}^{\infty} A_{n'} \cos[K_{n'}(x+d_s)] \cos[\beta_{n'}(y+w_s/2)], \quad (5)$$

where  $K_{n'}^2 = \omega^2/c^2 - \beta_{n'}^2$ ,  $\beta_{n'} = \pi n'/w_s$ , and the other fields are given by  $E_x^s = -(j/\omega\epsilon_0)\partial H_z^s/\partial y$  and  $E_y^s = (j/\omega\epsilon_0)\partial H_z^s/\partial x$ .

Our solution procedure is to choose one of the orthogonal modes in the slot, that is, a specific  $n'$ , and find the coefficients of the field components in the interaction region to satisfy the boundary conditions across the gap. Specifically, the continuity of  $E_y$  and  $H_z$  across the gap is required. That is, for  $E_y$ ,

$$\sum_{n=-\infty}^{\infty} A_n K_n \sin(K_n a) e^{-j\beta_n y} = \begin{cases} -A_{n'} K_{n'} \sin(K_{n'} d_s) \cos[\beta_{n'}(y+w_s/2)], & -w_s/2 < y < w_s/2 \\ 0, & w_s/2 < |y| < d_{N_s}/2, \end{cases} \quad (6)$$

and for  $H_z$ ,

$$\sum_{n=-\infty}^{\infty} A_n \cos(K_n a) e^{-j\beta_n y} = A_{n'} \cos(K_{n'} d_s) \cos[\beta_{n'}(y+w_s/2)], \quad -w_s/2 < y < w_s/2. \quad (7)$$

The dispersion relation  $\omega(\beta_0)$  is determined by multiplying Eq. (6) by the eigenfunctions in the interaction region,  $e^{j\beta_n y}$ , and integrating from  $-d_{N_s}/2$  to  $d_{N_s}/2$  and multiplying Eq. (7) by the eigenfunctions in the slot region,  $\cos[\beta_{n'}(y+w_s/2)]$ , and integrating from  $-w_s/2$  to  $w_s/2$ . The dispersion relation for the empty waveguide<sup>15</sup> becomes

$$D_{n'}(\omega, \beta_0) \equiv \begin{cases} 1 & \text{if } n' = 0 \\ 1/2 & \text{if } n' \neq 0 \end{cases} \times \frac{\cot(K_{n'} d_s)}{K_{n'} w_s} + \sum_{n=-\infty}^{\infty} \frac{\cot(K_n a)}{K_n d_{N_s}} F_{n, n'} = 0, \quad (8)$$

where

$$F_{n,n'} = \frac{1}{4} \left\{ \frac{\sin \left[ \frac{w_s}{2} (\beta_{n'} + \beta_n) \right]}{\frac{w_s}{2} (\beta_{n'} + \beta_n)} + (-1)^{n'} \frac{\sin \left[ \frac{w_s}{2} (\beta_{n'} - \beta_n) \right]}{\frac{w_s}{2} (\beta_{n'} - \beta_n)} \right\}^2. \quad (9)$$

Specifically for the  $n' = 0$  slot mode, the dispersion relation<sup>16</sup> becomes

$$D_0(\omega, \beta_0) = \frac{\cot \left( \frac{\omega d_s}{c} \right)}{\frac{\omega}{c} w_s} + \sum_{n=-\infty}^{\infty} \frac{\cot(K_n a)}{K_n d_{N_s}} \left( \frac{\sin \left\{ \frac{w_s \beta_n}{2} \right\}}{\frac{w_s \beta_n}{2}} \right)^2 = 0. \quad (10)$$

For this slot mode, which is a TEM mode in the slot, the electric field across the gap is  $E_y^s(0, y) = -(jA_0/\epsilon_0 c) \sin(\omega d_s/c)$ , a spatially constant electric field.

## B. Beam-waveguide linear stability analysis

The analysis of the slotted waveguide when the electron beam is present is based on the assumption that the beam only slightly perturbs the empty waveguide fields. The electron beam in the cartesian model [Fig. 1(b)] is a thin sheet beam of uniform density,  $n_b = n_s \delta(x - x_b)$ , located a distance  $x_b$  from the slot. The beam travels with a velocity across the slots given by  $V_B = V_0 \hat{a}_y$ . The relativistic mass ratio of this equilibrium beam is  $\gamma_0 = (1 - V_0^2/c^2)^{-1/2}$ .

The linear stability of the beam-waveguide system to small perturbations is examined as follows. The beam particles and resulting fields are perturbed according to  $\exp[j(\omega t - \beta_n y)]$  with a complex amplitude that depends on  $x$ . The perturbation produces fields of the form of TE waves. That is,  $\tilde{\mathbf{E}} = (\tilde{E}_x, \tilde{E}_y, 0)$  and  $\tilde{\mathbf{B}} = (0, 0, \tilde{B}_z)$ , all assumed to be small. The linearized equations of motion give

$$\begin{aligned} \tilde{v}_x &= - \frac{e}{jm\gamma_0\psi_n} [\tilde{E}_x + V_0 \tilde{B}_z], \\ \tilde{v}_y &= - \frac{e}{jm\gamma_0^3\psi_n} \tilde{E}_y, \\ \tilde{v}_z &= 0, \end{aligned} \quad (11)$$

where  $\psi_n = \omega - \beta_n V_0$  and all quantities with a tilde are small. The linearized continuity equation gives the perturbed beam density

$$\tilde{n} = - \frac{1}{j\psi_n} \frac{\partial}{\partial x} n_b \tilde{v}_x + \frac{n_b \beta_n}{\psi_n} \tilde{v}_y. \quad (12)$$

From these the perturbed charge and current density in Maxwell's equations can be computed. They are

$$\tilde{\rho} = -e\tilde{n} = \frac{e}{j\psi_n} \left[ \frac{\partial}{\partial x} (n_b \tilde{v}_x) - n_b j\beta_n \tilde{v}_y \right] \quad (13a)$$

and

$$\tilde{J}_x = -en_b \tilde{v}_x, \quad (13b)$$

$$\tilde{J}_y = -en_b \tilde{v}_y - eV_0 \tilde{n}. \quad (13c)$$

All perturbed quantities can be written in terms of the fields via Eq. (11). We now proceed to solve Maxwell's equations in the interaction space with the electron beam. We write the solutions for  $\tilde{H}_z$  in the form

$$\tilde{H}_z = \begin{cases} A_n \cos[K_n(a-x)] e^{-j\beta_n y}, & x_b < x < a \\ [B_n \cos(K_n x) + C_n \sin(K_n x)] e^{-j\beta_n y}, & 0 < x < x_b \end{cases}, \quad (14)$$

from which we can calculate  $\tilde{E}_x$  and  $\tilde{E}_y$ . We then apply the boundary conditions at the electron beam, which are: continuity of  $\tilde{E}_y$ , which gives

$$\frac{\partial \tilde{H}_z}{\partial x} \Big|_{x_b^+} = \frac{\partial \tilde{H}_z}{\partial x} \Big|_{x_b^-} \quad (15)$$

and jump in  $\tilde{H}_z$  due to the perturbed surface current, which gives

$$\tilde{H}_z(x_b^+) - \tilde{H}_z(x_b^-) = \frac{en_s \omega}{\psi_n} \tilde{v}_y(x_b). \quad (16)$$

These boundary conditions allow us to write all the fields in the interaction space in terms of one coefficient, say  $B_n$ . We then sum the fields over all these interaction space modes and match these fields to one of the modes in the slot, i.e., the  $n'$  mode as we did in Eqs. (6) and (7). From this we obtain a modified dispersion relation given by

$$\left\{ \begin{array}{l} 1 \text{ if } n' = 0 \\ 1/2 \text{ if } n' \neq 0 \end{array} \right\} \times \frac{\cot(K_{n'} d_s)}{K_{n'} w_s} + \sum_{n=-\infty}^{\infty} \frac{F_{n,n'}}{K_n d_{N_s}} \frac{\cos(K_n a) + \alpha K_n \cos(K_n x_b) \sin[K_n(a-x_b)]}{\sin(K_n a) + \alpha K_n \sin(K_n x_b) \sin[K_n(a-x_b)]} = 0, \quad (17)$$

where  $\alpha = e^2 n_s / m \epsilon_0 \gamma_0^3 \psi_n^2 \equiv (v/\gamma_0)(4\pi c^2/\gamma_0^2 \psi_n^2)$ . For the appropriate limit,  $v/\gamma_0 \ll 1$ , the first-order modified dispersion relation becomes

$$\begin{aligned} D_{n'}(\omega, \beta_0) &= \left\{ \begin{array}{l} 1 \text{ if } n' = 0 \\ 1/2 \text{ if } n' \neq 0 \end{array} \right\} \times \frac{\cot(K_{n'} d_s)}{K_{n'} w_s} + \sum_{n=-\infty}^{\infty} \frac{\cot(K_n a)}{K_n d_{N_s}} F_{n,n'} \\ &= - \frac{1}{d_{N_s}} \frac{v}{\gamma_0} \frac{4\pi c^2}{\gamma_0^2} \sum_{n=-\infty}^{\infty} \frac{1}{\psi_n^2} \frac{\sin^2[K_n(a-x_b)]}{\sin^2 K_n a} F_{n,n'} \end{aligned} \quad (18)$$

using Eq. (8). The left-hand side, when equal to zero, represents the empty waveguide dispersion relation and the right-hand side represents the electron beam effects.

We solve Eq. (18) in order to determine the interaction of the electron beam and the waveguide modes. We look for solutions where  $\omega = \beta_0 V_0 + \delta\omega$ , for  $|\delta\omega| \ll \beta_0 V_0 \equiv \omega_0$ . Expanding  $D_{n'}(\omega, \beta_0)$  about  $\omega_0$  and multiplying by  $(\delta\omega)^2$  we obtain from Eq. (18)

$$D_{n'}(\omega_0, \beta_0)(\delta\omega)^2 + \left. \frac{\partial D_{n'}}{\partial \omega} \right|_{\omega_0} (\delta\omega)^3 \simeq - \frac{1}{d_{N_s}} \frac{\nu}{\gamma_0} \frac{4\pi c^2}{\gamma_0^2} F_{0,n'} \frac{\sin^2[K_0(a - x_b)]}{\sin^2(K_0 a)}, \quad (19)$$

where we kept only the  $n = 0$  term on the right-hand side of Eq. (18), and  $K_0 = \sqrt{\omega_0^2/c^2 - \beta_0^2}$ . Equation (19) is solved and the results are displayed and discussed shortly. For the case of beam-waveguide resonance, i.e.,  $D_{n'}(\omega_0, \beta_0) = 0$ , Eq. (19) is a third-order equation for  $\delta\omega$  and possesses an unstable root of growth rate

$$\frac{\omega_I}{(\nu/\gamma_0)^{1/3}} = \frac{\text{Im } \omega}{(\nu/\gamma_0)^{1/3}} = \frac{\sqrt{3}}{2} \left\{ \frac{1}{\left. \frac{\partial D_{n'}}{\partial \omega} \right|_{\omega_0}} \frac{1}{d_{N_s}} \frac{4\pi c^2}{\gamma_0^2} F_{0,n'} \times \frac{\sin^2[K_0(a - x_b)]}{\sin^2(K_0 a)} \right\}^{1/3}. \quad (20)$$

Since this represents the maximum growth rate, all results are normalized to the factor  $(\nu/\gamma_0)^{1/3}$ . From Eq. (19), when the second-order term in  $\delta\omega$  dominates on the left-hand side (nonresonance), the stability of the mode is determined by the sign of  $D_{n'}(\omega_0, \beta_0)$ .

## C. Results

The results of the analytical analysis are presented in graphical form in Figs. 2–6. In Figs. 2 and 3, the empty slotted waveguide mode structure [Eq. (8)] for a 12 and 20 slot system is shown, and in Figs. 4–6 the linear growth rates [imaginary part of  $\delta\omega$  in Eq. (19)] are shown.

In Fig. 2, the dispersion relation for a 12 slot waveguide system is displayed. Referring to Fig. 1(b), the geometric parameters are:  $a = 2.5$  cm,  $d_{N_s} = 3.14$  cm,  $d_s = 1.0$  cm,  $w_s = 1.57$  cm. In Fig. 2(a), the dispersion relation of the system for the  $n' = 0$  slot mode is shown and for the  $n' = 1$  slot mode in Fig. 2(b). Specifically, frequency in GHz is plotted versus  $\beta_0 d_{N_s}$ , where  $\beta_0 d_{N_s} = 2\pi$  means the phase of the electric field across all slot gaps is in exactly the same direction at any time and when  $\beta_0 d_{N_s} = \pi$ , it means the field changes direction from gap to gap. For reference, the equivalent azimuthal harmonic number  $l$  for a cylindrical system is plotted along with  $\beta_0 d_{N_s}$ . Since the system is assumed to repeat itself every 12 slots, the spectrum is discrete, indicated by the "dots." If the system is not bounded in  $y$ , the dispersion curves are continuous as shown by the solid lines. Obviously, the dispersion curve repeats itself every  $2\pi$  in  $\beta_0 d_{N_s}$ . For reference, the beam wave  $\omega = \beta_0 V_0$  for a beam with  $\gamma_0 = 6$  is drawn which is very close to the velocity of light line on this graph. This value of  $\gamma_0$  corresponds to an electron energy of about 2.5 MeV. The experiments reported in the next section

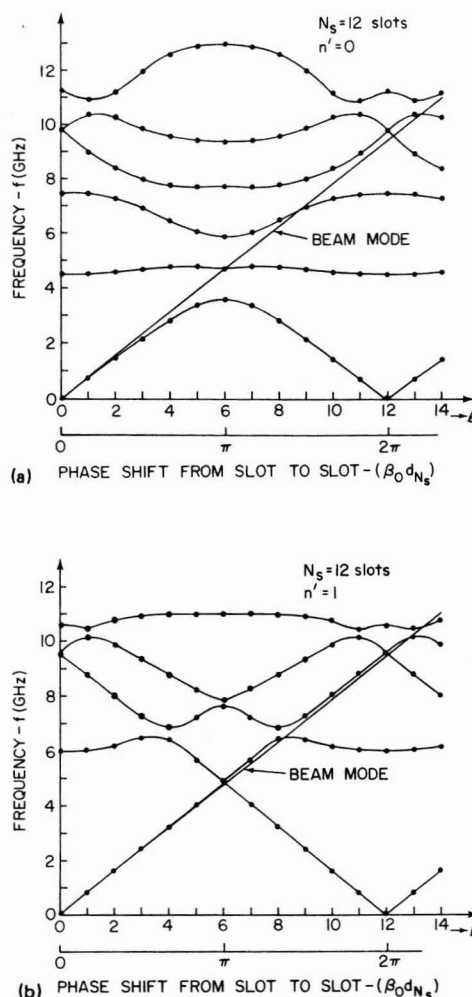


FIG. 2. Vacuum waveguide mode structure for a 12 ( $N_s$ ) slot periodic planar waveguide with geometry  $a = 2.5$  cm,  $d_{N_s} = 3.14$  cm,  $d_s = 1.0$  cm,  $w_s = 1.57$  cm. The interacting beam mode is also shown ( $\gamma_0 = 6$ ). (a)  $n' = 0$ : zero-order slot mode; (b)  $n' = 1$ : first-order slot mode.

were performed with injected electron beam energies in the range 2–2.5 MeV, with associated  $\gamma_0 = 5$ –6. We find these results to be relatively insensitive to variations in  $\gamma_0$  over this range. One should note that if no slots are present ( $d_s = 0$ ), the dispersion relation would be  $\omega = c\sqrt{k_y^2 + (n\pi/a)^2}$  and thus no modes have a phase velocity less than the velocity of light, and thus there can be no beam-waveguide mode resonant interaction. Obviously, the presence of the slots slows the waves down to below the velocity of light allowing resonant interaction. One can think of the various modes displayed in Figs. 2(a) and 2(b) as x-mode structure which is equivalent to radial ( $r$ ) mode structure in the cylindrical system.

In Fig. 3, the dispersion relation for a 20 slot waveguide system is displayed in the same manner as in Fig. 2. The

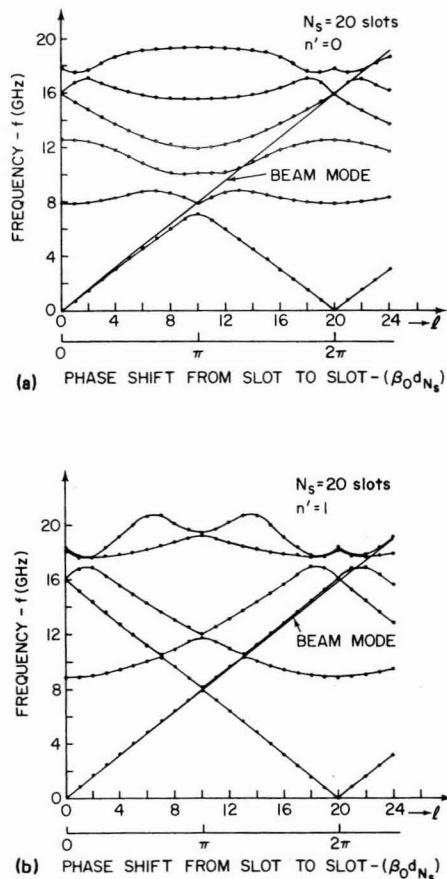


FIG. 3. Vacuum waveguide mode structure for a 20( $N_s$ ) slot periodic planar waveguide with geometry  $a = 1.7$  cm,  $d_{N_s} = 1.885$  cm,  $d_s = 0.4$  cm,  $w_s = 0.6283$  cm. The interacting beam mode is also shown ( $\gamma_0 = 6$ ). (a)  $n' = 0$ : zero-order slot mode; (b)  $n' = 1$ : first-order slot mode.

geometry of this system is,  $a = 1.7$  cm,  $d_{N_s} = 1.885$  cm,  $d_s = 0.4$  cm,  $w_s = 0.6283$  cm. The dispersion relation for the  $n' = 0$  slot mode is shown in Fig. 3(a) and for the  $n' = 1$  slot mode in Fig. 3(b). Again the beam mode ( $\gamma_0 = 6$ ) is displayed.

In Fig. 4, the normalized growth rate is shown for the 12 slot waveguide of Fig. 2 and an electron beam that is located 1.0 cm ( $x_b$ ) from the slots and has a relativistic mass ratio of  $\gamma_0 = 6$ . The normalization factor,  $\omega_c = 2\pi f_c$ , is that of an equivalent rotating beam at a radius of 6 cm. Specifically,  $f_c = 0.8$  GHz. The growth rate is plotted versus frequency  $f$  and equivalent azimuthal harmonic number  $l$  ( $\beta_0 d_{N_s}$ ). The growth rate for the  $n' = 0$  slot mode is displayed in Fig. 4(a) and for the  $n' = 1$  slot mode in Fig. 4(b). In Fig. 5, the normalized growth rate for a 12 slot waveguide is shown that has a slot width of half the value of that in Figs. 2 and 4, that is,  $w_s = 0.785$  cm. In Fig. 6, the normalized growth rate for a 20 slot waveguide is shown that has the same geometric values as in Fig. 3 and the same beam parameters as in Figs. 4 and 5.

For discussion purposes, consider the 12 slot guide whose mode structure appears in Fig. 2 and growth rate for

electron beam interaction in Fig. 4. For the  $n' = 0$  slot mode case, Fig. 2(a) indicates that there are beam mode-waveguide mode intersections in frequency and equivalent harmonic number at: 4–5 GHz ( $l \sim 6$ ), 6–7 GHz ( $l \sim 8$  or 9), 9–10 GHz ( $l \sim 12$ ), 10–11 GHz ( $l \sim 13$ ), etc. In Fig. 4(a), we see that there is strong interaction near these frequencies, indicated by finite growth rate and no unstable interaction at other harmonics. The frequency regime in Fig. 4(a) is extended beyond that shown in Fig. 2(a) but the same resonant interactions occur but with higher  $x$ -mode numbers. The growth rates are calculated as if the waveguide were not periodic, i.e., the dispersion relation represented by the solid line of Fig. 2(a). Though there is not exact intersection of a beam mode and a periodic waveguide mode (dots), we envision that a finite  $k_z$  will allow an intersection to occur. However, if the required  $k_z$  becomes too large, the frequency will be far removed from the spectrum regime displayed. The  $n' = 1$  slot mode results in Figs. 2(b) and 4(b) can be discussed in the same manner. However, one should note that the cutoff frequency in the slot is 9.6 GHz for this mode, and thus the two unstable interactions near  $l = 6$  and 8 in Fig. 4(b) represent attenuated waves in the slots but for  $l \gtrsim 12$  there are propagating modes in the slot. Clearly  $n' \geq 2$  slot modes have a higher cutoff frequency in the slot and thus are not displayed, because we surmise that attenuated slot modes will not be observed.

A 12 slot waveguide with a slot width of half that used in Figs. 2 and 4 results has a growth rate spectrum in frequency as shown in Fig. 5(a) for the  $n' = 0$  slot mode, and for the  $n' = 1$  in Fig. 5(b). The cutoff frequency in the slot is about 19 GHz for this width and thus all  $n' = 1$  growth rates represent attenuated waves in the slot.

The results of the 20 slot guide are shown in Figs. 3 and 6. Again, unstable interaction occurs where the beam wave intersects the waveguide mode. The  $n' = 1$  mode has a cutoff frequency in the slot of about 24 GHz indicating that only the unstable interactions above this value while propagate out of the system.

These results should be compared with those of the smooth hollow waveguide-electron beam interaction presented in Ref. 10. In those results, all beam harmonics ( $l$ ) were unstable once resonant interaction could occur, whereas in the present analysis, the guide mode structure does not allow for every  $l$  mode to resonantly interact.

### III. EXPERIMENT

#### A. Apparatus

In our configuration, a rotating relativistic  $E$ -layer is produced by passing a hollow nonrotating beam through a narrow symmetric magnetic cusp. The downstream chamber, in which the rotating beam propagates, has a conducting wall structure that is similar to that of the magnetron. The experimental configuration is shown schematically in Fig. 7. A hollow, nonrotating, relativistic electron beam (2–2.5 MeV, 20 kA, 30 ns) is emitted from a 12-cm-diam circular knife-edge carbon cathode located 7.5 cm upstream of the anode. A 0.5-cm-wide circular slit in the anode plate allows a fraction of the diode current to pass through the

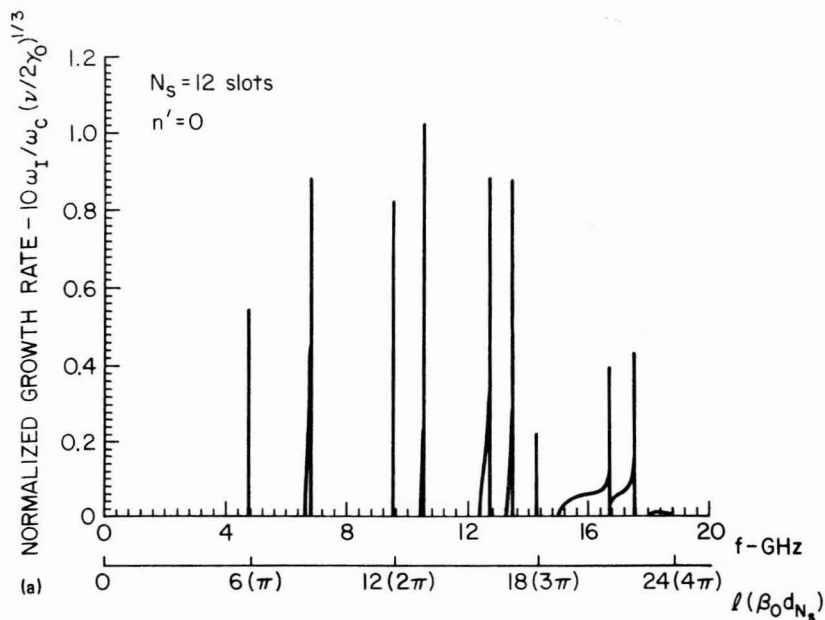
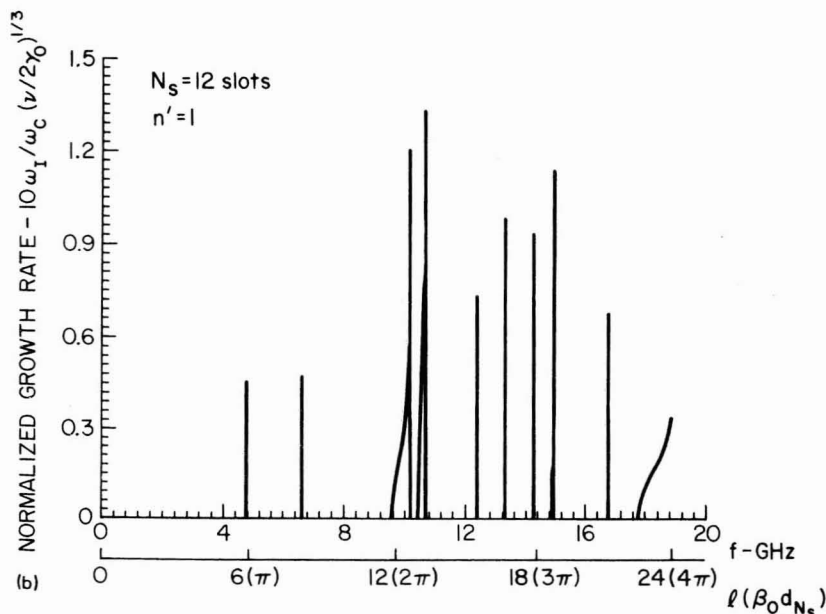


FIG. 4. Normalized TE growth rate [Eq. (19)] vs frequency  $f$  and equivalent harmonic number  $l$  for a 12 slot periodic planar waveguide with geometry the same as in Fig. 2 and beam parameters  $\gamma_0 = 6$ ,  $x_b = 1.0$  cm, and  $f_c = \omega_c/2\pi = 0.8$  GHz. (a)  $n' = 0$ : zero-order slot mode; (b)  $n' = 1$ : first-order slot mode.



anode plane into the magnetic cusp transition region, where the  $v_z \times B_r$  force efficiently converts axial particle velocity to azimuthal velocity downstream of the cusp transition. The details of particle motion in the cusp region are reported elsewhere,<sup>14</sup> and it is easily shown that the downstream particle orbits are axis encircling with a gyroradius equal to the cathode radius. Typical downstream beam parameters are 2 MeV, 2 kA, and 5 ns, and the rotating  $E$ -layer moves through the downstream region with an axial velocity in the range 0.1–0.3  $c$ . Thus, since the azimuthal velocity  $v_1 \approx c$ , the ratio  $v_1/v_{||}$  is in the range 3–10. The instantaneous ener-

gy spread in the electron beam is very small (less than 1%) as indicated from previous results.<sup>9</sup> The magnetic field upstream and downstream of the cusp transition is in the range 1200–1400 G, with a resultant relativistic cyclotron frequency of about 770 MHz at 1350 G.

#### B. Radiation at $12 \omega_c$

The rotating electron beam in the region downstream of the cusp transition interacts with an *outer* conducting slotted boundary as depicted in Fig. 7. It consists of 12 resonators ( $N_s = 12$ ) having an outer radius  $R_0$  of 7.5 cm and an inner



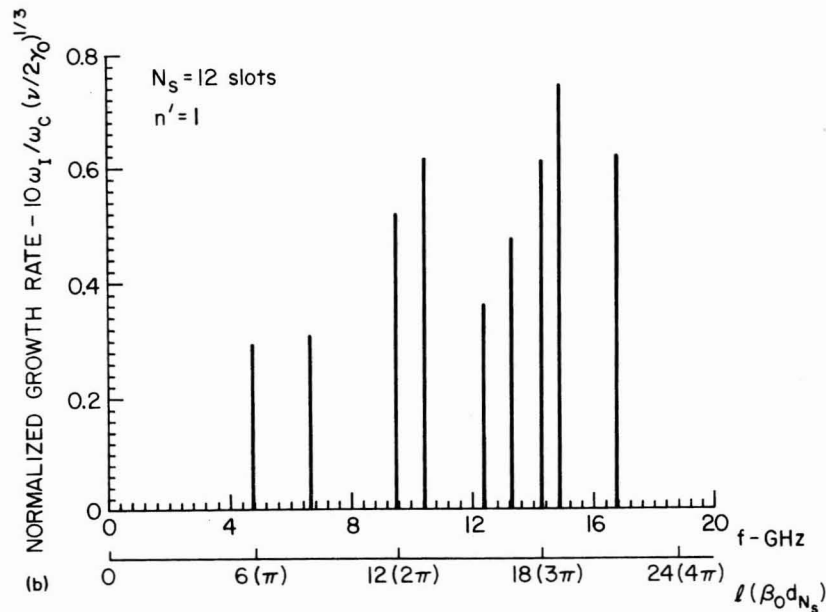
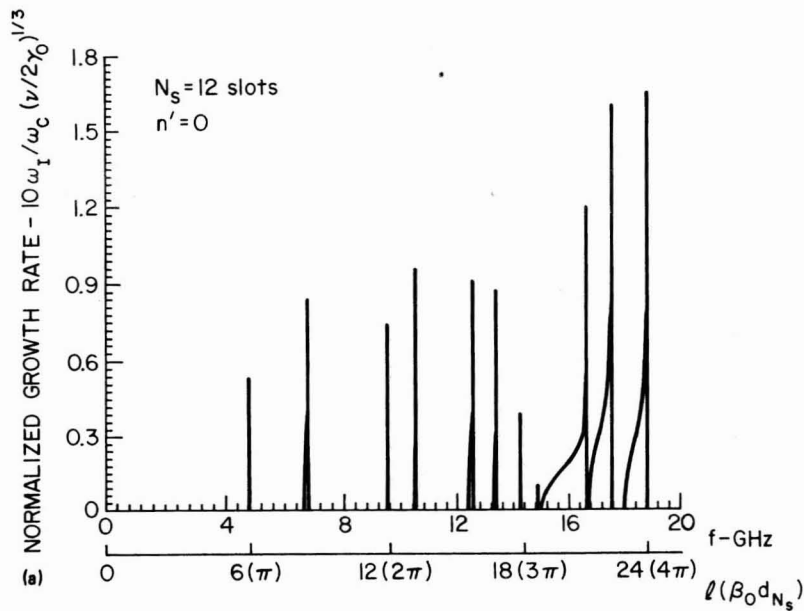


FIG. 5. Normalized TE growth rate [Eq. (19)] vs frequency  $f$  and equivalent harmonic number  $l$  for a 12 slot periodic planar waveguide with geometry the same as is Fig. 2 except  $w_s = 0.785$  cm. The beam parameters are  $\gamma_0 = 6$ ,  $x_b = 1.0$  cm, and  $f_c = \omega_c/2\pi = 0.8$  GHz. (a)  $n' = 0$ : zero-order slot mode; (b)  $n' = 1$  first-order slot mode.

radius of 6.5 cm, that is, the slot depth is 1 cm. No inner conducting boundary was used for these experiments. For comparison purposes, measurements were also made of the radiation produced when the beam interacts with a simple cylindrical outer conducting boundary of 7.5 cm radius. Details of the radiation production in this latter configuration have been reported elsewhere.<sup>9,10</sup> Unlike a conventional magnetron, where radiation is usually extracted through a window in one of the resonators, radiation in this system was extracted axially out the downstream end of the drift chamber, as shown in Fig. 7. The downstream end of the

drift chamber was flared to provide a smooth transition to free space, and the radiated power was detected by a receiving horn and a 34-m X-band (8–12 GHz) dispersive line connected to a calibrated attenuator and a calibrated detector. Total power was obtained by determining the effective radiation area at a given axial position of the receiving horn (by carefully surveying the region to determine over what area radiation is produced) from the output end of the drift chamber and multiplying the measured radiated power at the detector by the ratio of this area to that of the receiving horn. The power spectrum of the radiation was determined

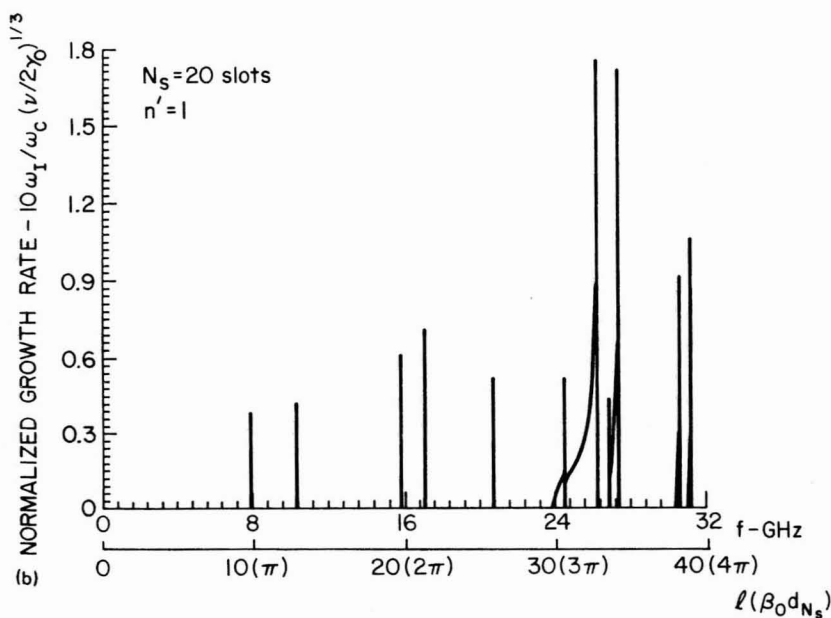
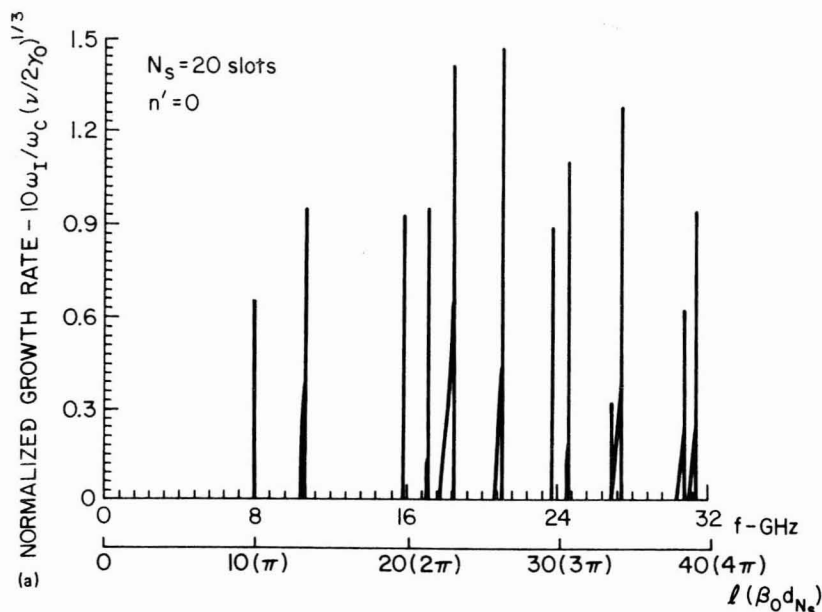


FIG. 6. Normalized TE growth rate [Eq. (19)] vs frequency  $f$  and equivalent harmonic number  $l$  for a 20 slot periodic planar waveguide with geometry the same as in Fig. 3 and beam parameters  $\gamma_0 = 6$ ,  $x_b = 1.0$  cm, and  $f_c = \omega_c/2\pi = 0.8$  GHz. (a)  $n' = 0$ : zero-order slot mode; (b)  $n' = 1$ : first-order slot mode.

by making use of the frequency-dependent group velocity of the radiation down the dispersive line. The undispersed radiation pulse duration was measured to be about 5 ns.

Results of these measurements are shown in Fig. 8 both for the simple cylindrical outer boundary [Fig. 8(a)] and for the magnetron-type boundary [Fig. 8(b)]. Each spectrum was obtained from a single shot, with each point representing a peak in the dispersed radiation waveform reaching the detector. The magnetic field setting in each case was 1350 G. Shot to shot reproducibility using the magnetron boundary was about  $\pm 5\%$  in frequency and about  $\pm 20\%$  in power

amplitude. It is easily seen that both the total power and the spectrum of the emitted radiation are affected dramatically by the multiresonator boundary. For the simple outer boundary, the power is very broad band in the X-band frequency spectrum with peak powers around 200 kW. However, for the magnetron type boundary, the peak power is a factor of 1000 greater and occurs predominantly at a single frequency around 9.6 GHz. These results have been published previously.<sup>8</sup>

An indication of the strength of the resonant interaction is shown in Fig. 9, where the power produced at 9.6



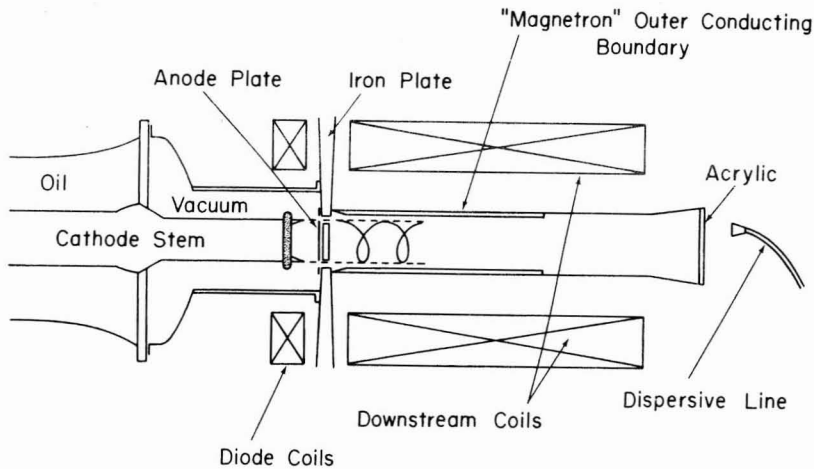


FIG. 7. General experimental configuration.

GHz is shown as a function of applied magnetic field. It is easily seen that only for magnetic fields close to 1350 G are these high powers obtained. The cusp cutoff field is the value above which the electrons no longer have sufficient energy to pass through the cusp.

### C. Radiation at $20 \omega_c$

Because of the difficulty in machining outer magnetron-type conducting boundaries for operation at higher frequencies, these experiments were conducted using slotted inner conductors, as shown in Fig. 1(a). Outer magnetron boundaries should, however, be superior for long pulse oper-

ation of this device, because electrons move to smaller radii as they lose energy and may eventually collide with an inner boundary, producing plasma and breakdown difficulties. Apart from this change, the basic experimental configuration in this case was the same as that used for studies at  $12 \omega_c$ , except that radiation was monitored using a 36-m Ku band (12–18 GHz) dispersive line with associated attenuators and detectors.

Tracings of raw oscilloscope data obtained from the Ku-band dispersive line for a simple coaxial boundary system and a slotted inner  $n = 20$  boundary system (of similar dimension) are shown in Fig. 10. It is easily seen that the broad band radiation observed in the unslotted boundary system is converted by the slotted boundary into higher power radiation at a single frequency. The attenuation values given include the correction for the fraction of the total area over which radiation is observed that is detected by the receiving horn, but do not include the frequency-dependent attenuation of the dispersive line. At 16 GHz, this attenuation is about 12 dB. As the burst duration is comparable to the pulse duration, the line bandwidth cannot be estimated accurately, although it is certainly less than 1 GHz. The best results obtained from these measurements are plotted in Fig. 11, and show the same characteristic behavior as the  $12 \omega_c$  results, although the radiated power is lower. This is attri-

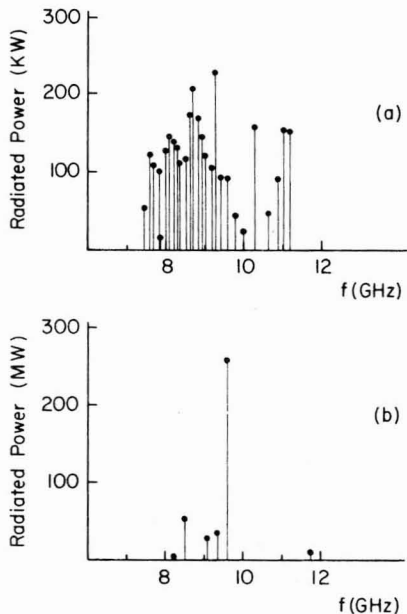


FIG. 8. Typical single shot power spectra for (a) simple cylindrical outer conducting boundary,  $R_0 = 7.5$  cm; (b)  $N_r = 12$  multiresonator magnetron outer conducting boundary,  $R_0 = 7.5$  cm,  $R_i = 6.5$  cm. Applied magnetic field is 1350 G in each case.

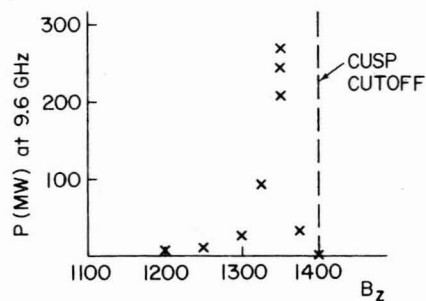


FIG. 9. Radiated power at 9.6 GHz plotted as a function of applied magnetic field.

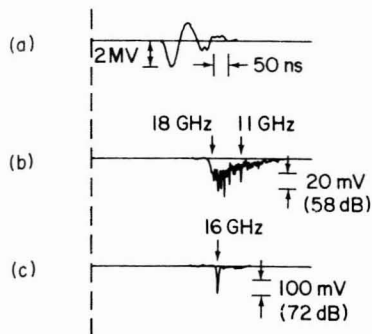


FIG. 10. Typical oscilloscope waveforms of (a) electron beam generator output voltage, (b) Ku band detector signal for rotating beam interacting with a simple coaxial boundary,  $R_o = 7.0$  cm,  $R_i = 5.0$  cm, (c) Ku band detector signal for a  $N_s = 20$  slotted inner conductor,  $R_o = 7.0$  cm,  $R_i = 5.3$  cm,  $d_s = 4$  mm,  $w_s = 6.3$  mm.

buted to a somewhat lower injection current (1 kA compared to 1.5–2 kA in the  $12\omega_c$  case) and to the fact that the fields in the slot cannot penetrate as far into the beam when the slots are smaller. It is also notable that this boundary was designed to operate with the “ $2\pi$ ,”  $n' = 0$  modes only, while the  $12\omega_c$  boundary may actually be resonating at a “ $2\pi$ ,”  $n' = 1$  mode.

In these experiments, we have routinely monitored radiation in X-band as well. In the case where a system is effectively radiating in the “ $2\pi$ ” mode at 16 GHz, we do not observe any enhancement of radiation in X-band that might be associated with excitation of the “ $\pi$ ” probe at 8 GHz. The

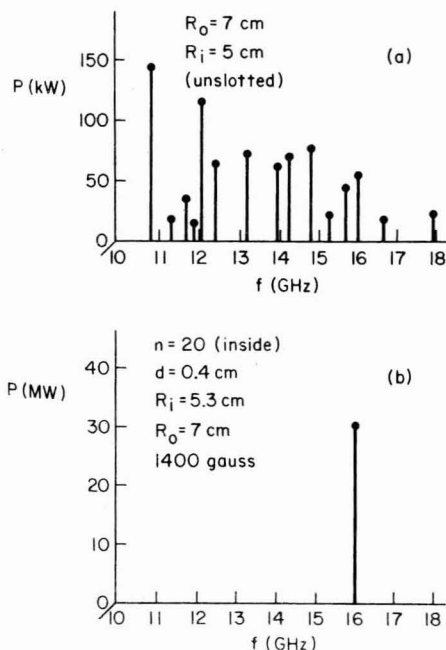


FIG. 11. Radiated power vs frequency (a) for the simple coaxial boundary, (b) for the  $N_s = 20$  slotted inner conductor.

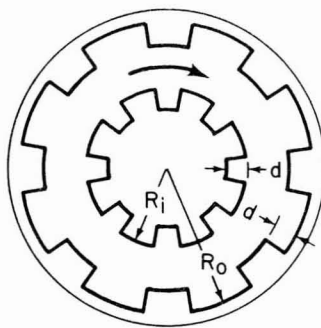


FIG. 12. Rotating beam propagating between slotted inner and outer boundaries.

observed radiation in X-band is more characteristic of that observed in an unslotted cylindrical boundary system.

We have also varied the slot depth to observe its effect on radiated power. As expected, unless the slot depth is set to a value such that a “ $2\pi$ ” resonance occurs near  $N_s\omega_c$ , peaking and enhancement of the radiated power spectrum at this frequency do not occur.

#### D. Radiation from “glide symmetric” boundaries

In this configuration, shown in Fig. 12, a rotating beam propagates between slotted boundaries with an effective  $180^\circ$  phase difference between inner and outer slots. In linear systems, such configurations are said to possess “glide reflection symmetry,” and theoretical analysis<sup>15</sup> shows that as the two conductors are moved closer together, the effective periodicity of the system approaches half that possessed by either boundary. Thus, in principle, such a configuration might lead to higher frequency radiation. When a beam was injected into such a configuration, the radiation was moved into Ka band (26–40 GHz) and was measured using a 36-m-long Ka band dispersive line. Radiation was produced predominantly at 36 GHz, slightly greater than  $40\omega_c$ , and the radiated power spectrum is shown in Fig. 13. Theoretical analysis of this system is currently in progress.

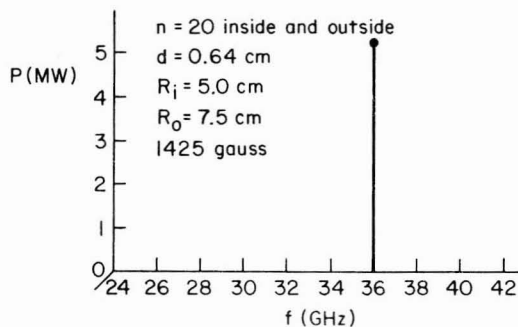


FIG. 13. Radiated power vs frequency for a rotating beam propagating between  $N_s = 20$  slotted inner and outer boundaries,  $R_o = 7.5$  cm,  $R_i = 5.0$  cm,  $d = 6.4$  mm.

#### IV. CONCLUSIONS

(1) Good qualitative agreement between theory and experiment has been achieved in these studies of the interaction of a rotating electron beam with a slotted wall waveguide structure that is placed either inside or outside of the electron beam.

(2) The slotted wall structures peak the radiation at selected frequencies versus the broad band nature of the radiation when a smooth wall structure is used. These selected frequencies are very close to the resonant frequencies where a beam mode intersects a waveguide mode.

(3) One would expect, because of the wall structure, that the beam would preferentially radiate at the  $2\pi$  mode, that is, the beam harmonic  $l$  that equals the number of slots. This is true if there is an intersection of a beam wave and a waveguide mode at this location. Thus, by changing wall geometry, this required intersection can be achieved and radiation is observed near  $l\omega_c$ .

(4) In order that multi-moding be reduced, the  $n' \geq 1$  slot mode cutoff frequency can be raised above the  $n' = 0$   $2\pi$  mode by reducing the width of the slots, that is, making  $w_s/d_{N_s}$  smaller. At the same time, however, the volume of the slots is reduced, which may affect the total radiated energy. Multimoding due to electron beam properties is less likely in our system than in conventional cross-field devices, because there is almost no velocity shear across the beam. This velocity shear gives rise to many  $\omega = \beta_0 V_0$  lines instead of the one we drew, that is, an angular region on the  $\omega$  vs  $\beta_0 d_{N_s}$  graph.

#### ACKNOWLEDGMENTS

We would like to acknowledge discussions in this work with K. R. Chu, J. Y. Choe, Y. Y. Lau, W. Namkung, M. J. Rhee, and H. S. Uhm. This work is supported by the Air Force Office of Scientific Research and the University of Maryland Computer Science Center.

- <sup>1</sup>V. A. Flyagin, A. V. Gapanov, M. I. Potelin, and V. V. Yulpatov, IEEE Trans. Microwave Theory Tech. **MTT-25**, 514 (1977).
- <sup>2</sup>J. L. Hirschfield and V. L. Granatstein, IEEE Trans. Microwave Theory Tech. **MTT-25**, 528 (1977).
- <sup>3</sup>H. S. Uhm, R. L. Davidson, and K. R. Chu, Phys. Fluids **21**, 1877 (1978).
- <sup>4</sup>D. A. G. Deacon, L. R. Elias, J. M. M. Madey, G. J. Ramian, H. A. Schwettman, and T. I. Smith, Phys. Rev. Lett. **38**, 897 (1977).
- <sup>5</sup>E. Ott and R. V. Lovelace, Appl. Phys. Lett. **27**, 378 (1975).
- <sup>6</sup>G. Bekefi and T. J. Orzechowski, Phys. Rev. Lett. **37**, 379 (1976).
- <sup>7</sup>A. Palevsky and G. Bekefi, Phys. Fluids **22**, 986 (1979).
- <sup>8</sup>W. W. Destler, R. L. Weiler, and C. D. Striffler, Appl. Phys. Lett. **38**, 570 (1981).
- <sup>9</sup>W. W. Destler, D. W. Hudgings, M. J. Rhee, S. Kawasaki, and V. L. Granatstein, J. Appl. Phys. **48**, 3291 (1977).
- <sup>10</sup>W. W. Destler, H. Romero, C. D. Striffler, R. L. Weiler, and W. Namkung, J. Appl. Phys. **52**, 2740 (1981).
- <sup>11</sup>Y. Y. Lau and L. R. Barnett, Int. J. Infrared Millimeter Waves **3**, 619 (1982).
- <sup>12</sup>Y. Y. Lau and L. R. Barnett, Int. J. Electron. **53**, 6 (1982).
- <sup>13</sup>H. S. Uhm, C. M. Kim, and W. Namkung, Phys. Fluids, (to be published).
- <sup>14</sup>M. J. Rhee and W. W. Destler, Phys. Fluids **17**, 1574 (1974).
- <sup>15</sup>R. Mittra and S. Laxpati, Can. J. Phys. **43**, 353 (1965).
- <sup>16</sup>G. B. Collins, *Microwave Magnetrons* (McGraw-Hill, New York, 1948), p. 56.